PHOTONICS Research

Resonance cavity-enhanced all-optical switching in a GdCo alloy absorber

YUNQING JIANG,[1,2,†] XIAOQIANG ZHANG,[1,2,†,*] HOUYI CHENG,[1,2,†] HUAN LIU,[3] YONG XU,[1,2,6] ANTING WANG,[4] CONG WANG,[1] STÉPHANE MANGIN,[5] AND WEISHENG ZHAO[1,2]

[1]School of Integrated Circuit Science and Engineering, Hefei Innovation Research Institute, Beihang University, Beijing 100191, China
[2]Anhui High Reliability Chips Engineering Laboratory, Hefei 230013, China
[3]School of Energy and Power Engineering, Beihang University, Beijing 100191, China
[4]Department of Optics and Optical Engineering, University of Science and Technology of China, Hefei 230026, China
[5]Institut Jean Lamour, UMR CNRS 7198, Universite de Lorraine, Nancy 54011, France
[6]e-mail: yongxu@buaa.edu.cn
[†]These authors contributed equally to this work.
*Corresponding author: xqzhang@buaa.edu.cn

In spintronic applications, there is a constant demand for lower power consumption, high densities, and fast writing speed of data storage. All-optical switching (AOS) is a technique that uses laser pulses to switch the magnetic state of a recording medium without any external devices, offering unsurpassed recording rates and a simple structure. Despite extensive research on the mechanism of AOS, low energy consumption and fast magnetization reversing remain challenging engineering questions. In this paper, we propose a newly designed cavity-enhanced AOS in GdCo alloy, which promotes optical absorption by twofold, leading to a 50% reduction in energy consumption. Additionally, the time-resolved measurement shows that the time of reversing magnetization reduces at the same time. This new approach makes AOS an ideal solution for energy-effective and fast magnetic recording, paving the way for future developments in high-speed, low-power-consumption data recording devices. © 2023 Chinese Laser Press

https://doi.org/10.1364/PRJ.497939

1. INTRODUCTION

With the rapid development of cloud computing, big data, and artificial intelligence over the past few decades, the demand for more energy-efficient, higher density, and faster methods to record data has been an exciting frontier [1,2]. Unlike traditional hard-disk recording, to realize ultrahigh recording densities above 1 Tb/in.², which needs a magnetic field much larger than those generated by a write head, the technology in which a laser is used to heat the recording medium and reduce the magnetization during the recording process is a good strategy [3]. This technology is called "heat-assisted magnetic recording" (HAMR), which can decrease the switching field down to a reasonable value, and a petabyte recording density has been realized [4]. However, the recording head relying on a current to generate a magnetic field is still indispensable. Recently, all-optical switching (AOS), where a laser pulse can switch the magnetic state of a recording medium to the opposite direction without any external devices, including a magnetic field, has attracted investigators to explore it experimentally and theoretically [5–7]. Compared with traditional recording technologies, including the HAMR, the AOS has the advantages of unsurpassed recording rates and simple structure [8–12]; it also

has been found in many ferrimagnetic films, e.g., TbCo, GdFeCo [13–16].

As ferrimagnetic metallic materials, GdCo alloys, which have antiferromagnetic exchange coupling formed by the magnetic moments of the rare-earth Gd and the transition metal Co, are widely used in magnetic-optical recording [17–19]. In the past few years, AOS has been found in GdCo alloys as well; meanwhile, its switching mechanism has been investigated abundantly, which is the different spin dynamics of the rare-earth Gd and the transition metal Co, where the transition metal reaches the zero net magnetization state much faster than the rare-earth component [20,21]. During the study of the AOS mechanism, however, little attention has been paid to reducing its energy and time consumptions, which have come to the forefront of its future application [22]. Recently, by fabricating Au nanoislands at the surface of magnetic films, Cheng *et al.* reported the plasmon-enhanced AOS and realized an 18.5% energy reduction [23]. However, the uneven nanoislands attenuate most of the incident light, and only the gaps between Au nanoislands can enhance the electric field intensity, resulting in the uneven magnetization switching of the magnetic films, which is not better for uniform data storage

[24]. In the same year, Kim *et al.* realized high-visibility magneto-optical Kerr effect (MOKE) microscopy by designing extreme antireflection [25], which provides a possibility to reduce the power dissipation and achieve uniformity of AOS. Perfect absorption of electromagnetic energy as an efficient method is widely used on suppressing the light reflection and transmission. Fabry–Perot cavity with metal-insulator-metal structure can generate cavity resonance with tunable wavelength of incident light and polarization insensitive [26–28]. As a lossy material, the thickness of the GdCo alloy and the inserted dielectric layer can affect the optical absorption. To obtain better all-optical switching of the GdCo layer, the net magnetization of GdCo layer needs to be found after ascertaining the thickness of the GdCo alloy and the optical cavity.

To fully use the pump energy and reduce the energy consumption, in this paper, a dielectric layer is deposited between an Au layer with the thickness of 20 nm and a ferrimagnetic thin film (FTF). By designing the thickness of the dielectric layer between the FTF and the Au layer, a resonant cavity is formed, and the energy consumed by AOS is reduced by 50%. In addition, by testing with a time-resolved magneto-optical Kerr effect (TR-MOKE) system, the recording speed is also promoted. We believe that this energy- and time-efficient design can pave the way for the practical application of AOS for data storage.

2. DESIGN OF THE RESONANCE CAVITY

When an optical beam passes through one medium into another medium, reflections and transmissions will appear, simultaneously, and the well-known Fresnel equations can be used to calculate the reflection and transmission coefficients [29]. Due to the impedance mismatch of two transmission lines, similar phenomena can also exist in a circuit, when an electric signal propagates from one transmission line to another line with a different impedance [30,31]. Thus, an equivalent circuit model, which is convenient and easier to understand, can be used to calculate the optical beam propagation in two or more inhomogeneous optical media [32]. As shown in Fig. 1(a), an optical beam with a wavelength of $\lambda = 780$ nm impinges on an FTF composed of Pt(2 nm)/GdCo(t_{GdCo})/Pt(2 nm)/Ta(3 nm) from the free space with refractive index $n_0 = 1$. t_{GdCo} is the thickness of the GdCo layer, and the FTF is deposited on a SiO$_2$ substrate. The effect of each layer of the FTF will be explained in the following. From the theory of the equivalent circuit model, the free space and substrate are equivalent to two transmission lines with an impedance of Z_0 and Z_{SiO2}, respectively. Meanwhile, the FTF with an impedance of Z_{FTF} can be regarded as a load attached to the junction between the two transmission lines, as shown in Fig. 1(c). According to the Maxwell equations, the impedance has the relation of $Z_{SiO2} = Z_0/n_{SiO2}$, where $n_{SiO2} = 1.54$ is the refractive index of the substrate. Then, the amplitude transmission and reflection coefficients can be calculated as [31]

$$t_1 = \frac{2}{1 + \kappa + (a + ib)}, \tag{1}$$
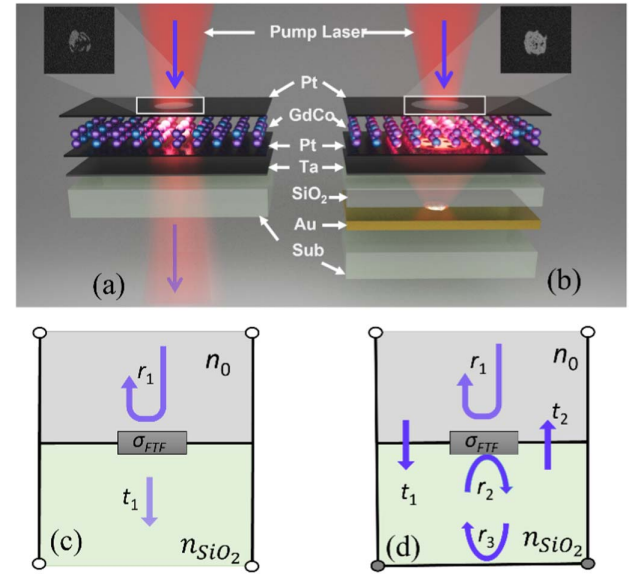
Fig. 1. Schematic of the AOS in (a) FTF and (b) CE-FTF. The FTF is composed of Pt/GdCo/Pt/Ta. Equivalent transmission line mode of (c) FTF and (d) CE-FTF. In the equivalent circuit model, the FTF is equivalent to a load with a conductivity of σ_{FTF}, and the added Au layer induces a short circuit. Insets show the magnetic domain state, where the black contrast corresponds to the initial magnetization, and the white contrast corresponds to a magnetization reversal.

$$r_1 = \frac{1 - \kappa - (a + ib)}{1 + \kappa + (a + ib)}. \tag{2}$$

To simplify Eqs. (1) and (2), the parameters κ, a, and b are introduced, where $\kappa = n_0/n_{SiO2}$, $a + ib = Z_0\sigma_{FTM}d_{STM}/n_0$, and $\sigma_{FTM} = 1/(Z_{FTM}d_{FTM})$ is the complex conductivity of the FTF, which can be calculated by using the equivalent circuit method (see Appendix A and Appendix B). Figure 2(a) shows the conductivity of the FTF as a function of the thickness of the GdCo alloy. Then, the optical absorption of the FTF can be obtained as

$$A = 1 - T - R = \frac{4a}{(1 + \kappa + a)^2 + b^2}, \tag{3}$$

where T and R are the transmittance and reflectance of the incident beam, and $T = \kappa|t|^2$, $R = |r|^2$, respectively [31]. In Eq. (3), considering the limiting case, the maximal absorption is $A_{max} = 1/(1 + \kappa)$, when $1 + \kappa = a$ and $b = 0$, concurrently. Therefore, the maximal absorption of the FTF cannot be larger than $1/2.54 \approx 40\%$. As shown in Appendix C, COMSOL Multiphysics is employed to calculate the optical absorptions of each layer of the FTF under different thicknesses of GdCo alloy. We can find that the total absorption of the FTF is always less than 40% [Fig. 2(b)]. More importantly, the optical absorption of GdCo alloy, which works as the recording film, is less than 35%, and most of the laser energy is wasted, causing high energy consumption of AOS.

To take advantage of the laser energy sufficiently and increase the optical absorption of GdCo alloy, a SiO$_2$ dielectric
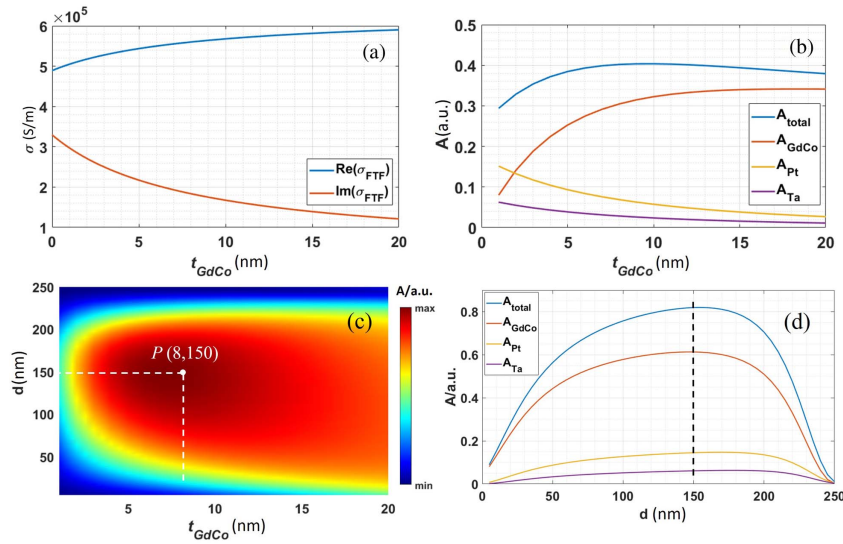
Fig. 2. (a) Conductivity of the FTF as a function of the thickness of the GdCo alloy, and the thicknesses of Pt and Ta layers are 2 and 3 nm, respectively. (b) Optical absorption of each layer and the total absorption of the FTF under different thicknesses of the GdCo alloy. (c) Phase diagram of the optical absorption of the GdCo alloy as a function of its thickness t_{GdCo} and the thickness of the inserted dielectric layer d. (d) Absorption of each layer of the CE-FTF under different thicknesses of the inserted dielectric layer d with the thickness of $t_{GdCo} = 8$ nm.

layer and an Au layer with a thickness of 20 nm are added between the FTF and the SiO$_2$ substrate, as shown in Fig. 1(b). A 20 nm Au layer is sufficient to meet the skin depth requirement at the pump laser frequency. The SiO$_2$ dielectric layer forms an optical cavity between the FTF and Au layer. In the new system, which is called "cavity-enhanced ferrimagnetic thin film" (CE-FTF) in the following, the Au layer can reflect the transmitting pump beam to the FTF again. Hence, by designing the thickness of the dielectric layer carefully, a resonance cavity with reflection coefficients of r_2 and r_3 can be obtained between the FTF and the Au layer. The equivalent circuit mode of the CE-FTF can be seen in Fig. 1(d). As shown in Fig. 1(d), because the thickness of the Au mirror is larger than its skin depth, the added Au layer causes a short circuit, where the reflection coefficient of the Au layer is $r_3 = -1$. From the analysis before, the reflection coefficient of r_2 is

$$r_2 = \frac{\kappa - 1 - (a + ib)}{1 + \kappa + (a + ib)}. \tag{4}$$

Based on the multiple interference theory (see Appendix D), the total reflection coefficient of the CE-FTF can be expressed as

$$r = r_1 - \frac{t_1 t_2 e^{i2\varphi}}{1 + r_2 e^{i2\varphi}}, \tag{5}$$

where φ is the propagation phase in the resonance cavity, and $\varphi = k_0 n_{SiO2} d$. Herein, k_0 is the free-space wavenumber, and $k_0 = 2\pi/\lambda$. In Eq. (5), t_2 is the transmission coefficient of the pump beam from the inserted SiO$_2$ dielectric layer to the free space, and it is

$$t_2 = \frac{2\kappa}{1 + \kappa + (a + ib)}. \tag{6}$$

Then, after simplification, the absorption of the CE-FTF is [31]

$$A = \frac{4a}{(1 + a)^2 + (b + \kappa \cdot \cot \varphi)^2}. \tag{7}$$

From Eq. (7), we can see that the absorption of this CE-FTF is a function of the conductivity of the FTF and the thickness of the dielectric layer, and it is easy to find that the maximal absorption of the CE-FTF is 100% when $a = 1$ and $b + \kappa \cdot \cot \varphi = 0$. Because of the impedance mismatch, 100% perfect absorption is difficult to realize. However, as shown in Fig. 2(a), the thicknesses of Pt and Ta layers are selected as 2 and 3 nm, respectively, and the whole conductivity of the FTF can be tuned by changing the thickness of the GdCo alloy. Thus, by designing the parameters of the CE-FTF carefully, the absorption of the GdCo alloy can be enhanced as well.

Next, the optical absorption performance of the CE-FTF is surveyed under different thicknesses of the GdCo alloy and the inserted dielectric layer (d). As shown in Fig. 2(c), at point P, where the thicknesses of the GdCo alloy and the insert dielectric layer are $t_{GdCo} = 8$ nm and $d = 150$ nm, the CE-FTF has a maximal optical absorption. Figure 2(d) shows the optical absorption of each layer of the CE-FTF under different thicknesses of the inserted dielectric layer with the thickness of $t_{CoGd} = 8$ nm. We can find the total absorption of the CE-FTF is larger than 80%; meanwhile, the absorption of the GdCo alloy layer has a maximal absorption of about 60% when $d = 150$ nm. Compared with the single FTF [Fig. 2(b)], where only about 30% of the incident power is absorbed by the GdCo alloy when $t_{CoGd} = 8$ nm, the absorption has about twofold enhancement.

3. SAMPLE PREPARATION AND MEASUREMENT SETUP

After trading off the thickness of the GdCo alloy and the optical cavity performance, the samples are prepared. First, to find the

net magnetization M_s of the FTF [33,34], a series of 8 nm thickness $Gd_X Co_{1-X}$ alloys with different composition ratios of Gd ranging from $X = 16\%$ to $X = 28\%$ were grown by a magnetron sputtering system (TREC-MS-700) from Truth Equipment Corporation, TREC. As shown in Fig. 1(a), the FTF has the following multilayer structure: substrate/ $Ta(3\,nm)/Pt(2\,nm)/Gd_X Co_{1-X}(8\,nm)/Pt(2\,nm)$. To achieve a strong perpendicular magnetic anisotropy (PMA) and prevent oxidation, two layers of Pt with a thickness of 2 nm were deposited on the top and bottom of the GdCo alloy, respectively, and the Ta layer works as a buffer layer [33,35]. Then, the normalized magnetic hysteresis loops of the grown samples with different composition ratios are tested by the Kerr rotation θ_k in a MOKE system with the polar configuration at room temperature [34]. As shown in Fig. 3(a), the measurement results confirm that the FTFs have PMA when X ranges from 16% to 24%. Figure 3(b) shows the coercive field H_c under the different Gd content, which is extracted from Fig. 3(a), and we can obtain the M_s at $X = 20\%$.

Until now, the finally optimized structure and parameters of the CE-FTF can be confirmed, and it is substrate/ $Au(20\,nm)/SiO_2(150\,nm)/Ta(2\,nm)/Pt(2\,nm)/Gd_{0.2}Co_{0.8}$ $(8\,nm)/Pt(2\,nm)$. Then, the final samples were prepared. Before depositing the FTF, the Au layer and the inserted SiO_2 dielectric layer were prepared first by atomic layer deposition. To explore the effect of the inserted dielectric layer, a series of samples with the different inserted layers d were grown, i.e., $d = 50, 100, 150,$ and 200 nm, respectively. On the other hand, to make a comparison, a pure ferrimagnetic thin film (PFTF) without an Au layer and an inserted layer was prepared as well. By using a home-built static MOKE imaging system, as shown in Fig. 8 in Appendix F, the domain states of the samples after illumination with a single linearly polarized laser pulse are measured. Before illumination, a magnet with a magnetic field larger than the H_c was applied to initialize the magnetization state of the sample. Figure 3(c) shows the magnetization of the PFTF and the CE-FTF with $d = 150$ nm

after illumination with different laser fluences, and the domain state can be distinguished by the white and black contrasts in the MOKE image. In Fig. 3(c), as for the PFTF, we can find almost no domain state switches when the laser fluence is less than 0.50 mJ/cm^2; as for the CE-FTF with $d = 150$ nm, the domain state can be switched at the fluence of 0.31 mJ/cm^2. With the increase of the laser fluence, the switching area is larger, and the CE-FTF can achieve almost a uniform magnetization switching when the fluence is 0.69 mJ/cm^2, while it is about 1.26 mJ/cm^2 for the PFTF. All the MOKE images of the samples after illumination with different laser fluences are shown in Fig. 9 in Appendix G. Compared with the other results, it is also clear to find that the four CE-FTFs have little switching fluence, which is reduced by about 50%.

4. ULTRAFAST MAGNETIZATION DYNAMICS OF THE CE-FTF

To further test the performance of the samples precisely, a TR-MOKE system with a temporal resolution better than 50 fs was employed to monitor the magnetization dynamics (see Fig. 10 in Appendix H). We detect Kerr rotation signal of its frequency component synchronized with an optical chopper by using a lock-in amplifier, and all measurements are repeatedly tested to ensure the accuracy of results. As shown in Fig. 10, the probe beam with a wavelength of about 400 nm is used to probe the dynamics of the magnetization of the samples after the heating of a line-polarized pump beam, and the fluence of the probe beam is far less than the pump beam. Figures 4(a) and 4(b) show the magnetization dynamic Kerr signals of the CE-FTF with $d = 150$ nm and the PFTF under different pump fluences, respectively. In the measurement, an external magnetic field that is larger than the H_c is applied to ensure the samples have the same initial magnetic state. As shown in Figs. 4(a) and 4(b), an ultrafast demagnetization caused by the pump laser can be found first; then, the magnetization relaxes and comes back to the initial state when the pump
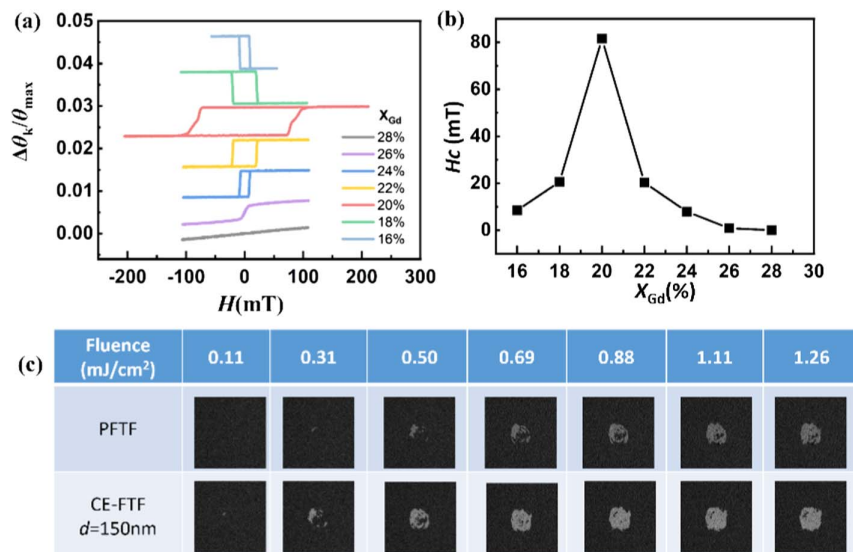
Fig. 3. (a) Normalized hysteresis loops and (b) coercive field H_c for the FTFs from MOKE with different composition ratios of Gd. (c) Static MOKE images of the PFTF and the CE-FTF with $d = 150$ nm after illumination with different laser fluences.
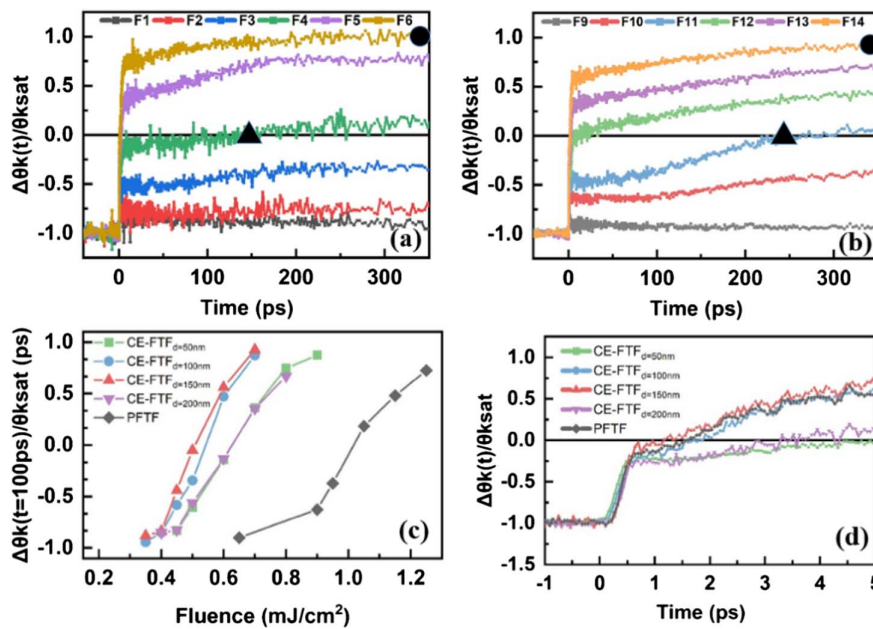
Fig. 4. Normalized ultrafast magnetization dynamics of (a) the CE-FTF with $d = 150$ nm and (b) the PFTF triggered by the pump beam with different fluences. (c) The normalized ultrafast magnetization dynamics of the PFTF and the four CE-FTFs measured at $t = 100$ ps under different laser fluences. (d) The normalized initial ultrafast magnetization dynamics of the PFTF triggered at the laser fluence of F_{14} and the four CE-FTFs triggered at the laser fluence of F_6, respectively. Here, $F_1 = 0.35$ mJ/cm^2, $F_2 = 0.40$ mJ/cm^2, $F_3 = 0.45$ mJ/cm^2, $F_4 = 0.50$ mJ/cm^2, $F_5 = 0.60$ mJ/cm^2, $F_6 = 0.70$ mJ/cm^2, $F_9 = 0.65$ mJ/cm^2, $F_{10} = 0.90$ mJ/cm^2, $F_{11} = 0.95$ mJ/cm^2, $F_{12} = 1.05$ mJ/cm^2, $F_{13} = 1.15$ mJ/cm^2, and $F_{14} = 1.25$ mJ/cm^2.

power is not high. With the increase of the pump fluence, a full magnetization reversal occurs. We can find that the threshold fluence (TF) is 0.50 mJ/cm^2 for the CE-FTF; as for the PFTF, it is 0.95 mJ/cm^2 [the triangle symbol in Figs. 4(a) and 4(b)]. We can also find that the consumed pump fluence is reduced by $(0.95 - 0.5)/0.95 = 47.4\%$. Meanwhile, the consumed time to fully demagnetized state is also decreased [reduced from 250 to 150 ps, as shown in Figs. 4(a) and 4(b)]. We define the time of reversing magnetization as the time reached maximum reversal. The time of reversing magnetization for the CE-FTF is within ≈ 200 ps, but the PFTF is more than 300 ps, as shown in Fig. 4. The normalized ultrafast magnetization dynamics of the four CE-FTFs with different inserted dielectric thicknesses can be found in Fig. 11 in Appendix I. In order to evaluate the performances of the samples systemically, the saturate magnetization reversal (SMR), which is defined as the final switched magnetization under a large pump fluence and after a long relaxation time, is studied; they are marked by a circle symbol, as shown in Figs. 4 and 11. The consumed pump fluences of the PFTF and the four CE-FTFs are summarized in Table 1. Compared with the PFTF and the CE-FTF with $d = 150$ nm, it is easy to find that the consumed pump fluence of the SMR is reduced about $(1.25 - 0.7)/1.25 = 44\%$. Considering that

magnetization reversal of the SMR of the PFTF is about 80%, it is about 84% for the CE-FTF with $d = 150$ nm. The lower power consumption is almost in accordance with the simulation as well.
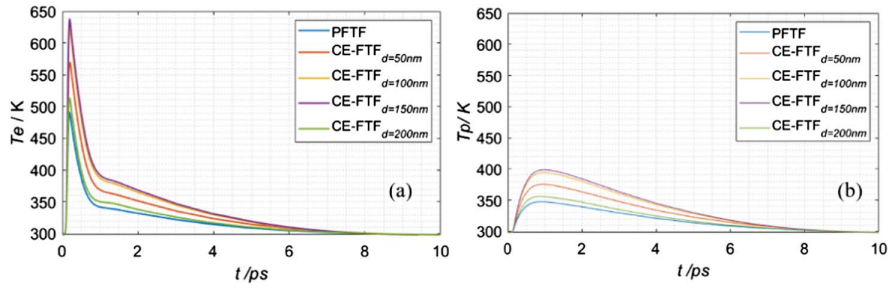
We also explore the normalized ultrafast magnetization dynamics of the PFTF and the four CE-FTFs measured at $t = 100$ ps, as shown in Fig. 4(c); they are extracted from Figs. 4(b) and 11 in Appendix I. We can find that all the four CE-FTFs have a lower laser fluence to reverse the magnetization, which means that the CE-FTFs have a higher efficiency of AOS. More importantly, the CE-FTF with $d = 150$ nm has the highest efficiency at the same laser fluence. From Table 1, in Figs. 4(a) and 11, regardless of the TF or the SMR, we can see that the CE-FTF with $d = 150$ nm has the preponderance of lower energy consumption and the highest magnetization reversal efficiency, which is the best for AOS.

5. PHOTOTHERMAL EFFECT DURING THE ULTRAFAST MAGNETIZATION REVERSAL

To demonstrate the magnetization manipulation process and certify the photothermal effect in the laser heating of the samples, the two-temperature model is applied to demonstrate the

Table 1. TF and the SMR of the PFTF and the Four CE-FTFs

Sample		PFTF	CE-FTF $d = 50$ nm	CE-FTF $d = 100$ nm	CE-FTF $d = 150$ nm	CE-FTF $d = 200$ nm
▲	TF	0.95 mJ/cm^2	0.60 mJ/cm^2	0.50 mJ/cm^2	0.50 mJ/cm^2	0.50 mJ/cm^2
●	SMR	1.25 mJ/cm^2	0.90 mJ/cm^2	0.70 mJ/cm^2	0.70 mJ/cm^2	0.80 mJ/cm^2
		(~80% reversal)	(~82% reversal)	(~84% reversal)	(~84% reversal)	(~67% reversal)

Fig. 5. Calculated (a) electron temperature and (b) phonon temperature of the PFTF and the four CE-FTFs under the same laser fluence.

electronic and phonon temperature dynamics, as shown in Appendix E [36]. Figure 5 shows the electron and phonon temperatures of the PFTF and the four CE-FTFs under the same fluence. We can see that the electron and the phonon temperatures are increased from room temperature to the maximum after the pump of the laser beam; then, they both relax back to room temperature. We can also find that the electron and phonon temperatures of the four CE-FTFs are larger than those of the PFTF; they are also easier to reach their maximum temperature within about 0.5 ps. In addition, the CE-FTF with $d = 150$ nm is the easiest to reach the maximum temperature, which is because it has a largest optical absorption. Figure 4(d) shows the normalized initial ultrafast magnetization dynamics of the four CE-FTFs triggered at the laser fluence of $F_6 = 0.70$ mJ/cm^2 and PFTF triggered at the laser fluence of $F_{14} = 1.25$ mJ/cm^2, respectively. In Fig. 4(d), two different behaviors, i.e., ultrafast demagnetization and rapid magnetization relaxation, can clearly be distinguished, and the ultrafast demagnetization is within about 0.5 ps. Meanwhile, the CE-FTF with $d = 150$ nm has the largest demagnetization than other samples, and the PFTF and CE-FTF with $d = 150$ nm have almost the same trend of magnetization dynamics because they have almost the same effective optical absorption. These results are well in account with the simulation of the two-temperature model. Thus, we can say that the CE-FTFs, especially the CE-FTF with $d = 150$ nm, have an enhancement in photothermal effect, which induces the lower consumed time of AOS.

6. CONCLUSION

In summary, a cavity-enhanced AOS, which is composed of a GdCo alloy and a SiO$_2$ dielectric layer deposited on an Au layer, is proposed in this paper. The equivalent circuit model is employed to explore the optical absorption of the CE-FTF; further, by optimizing the thickness of the inserted dielectric layer of the cavity and the thickness of the GdCo alloy, the energy consumed by AOS is reduced by about 50%. The optimized structure and parameters of the CE-FTF, which is substrate/Au(20 nm)/SiO$_2$(150 nm)/Ta(2 nm)/Pt(2 nm)/Gd$_{0.2}$Co$_{0.8}$(8 nm)/Pt(2 nm), are confirmed and prepared as well. We verify that the multilayer structure has a strong PMA and can achieve a uniform magnetization switching with a laser fluence less than 0.69 mJ/cm^2, which is reduced by about 50% than the PFTF. A TR-MOKE system is used to test the performance of the samples precisely, and it once more

affirms the low energy consumption of the CE-FTF. In addition, the magnetization switching speed, which is promoted, is also confirmed. The two-temperature model certifies that the enhancement in photothermal effect of the CE-FTF leads to a higher efficiency of magnetization switching. These excellent performances of CE-FTF make AOS an ideal way for energy-effective and fast magnetic recording and pave the way for its practical application.

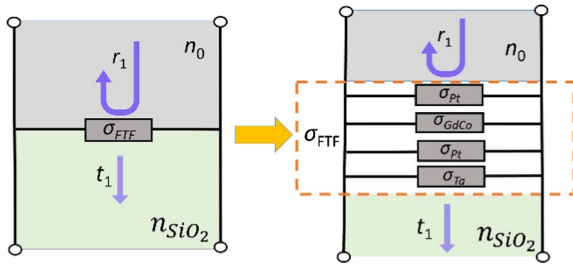## APPENDIX A: COMPLEX CONDUCTIVITY OF EACH LAYER OF THE FTF

For the FTF, the effective permittivity of each layer has the relationship of $\varepsilon = 1 + i\frac{\sigma}{\varepsilon_0 \omega}$, where σ is the complex conductivity, ε_0 is the permittivity of vacuum, and ω is the frequency of the incident beam [37]. The effective permittivity of each layer is also the square of their refractive indexes. From Refs. [21,36], the complex refractive indexes of each layer are $n_{\text{GdCo}} = 3.79 + 3.89i$, $n_{\text{Ta}} = 1.09 + 3.06i$, and $n_{\text{Pt}} = 2.85 + 4.96i$, respectively. Thus, the complex conductivity of GdCo, Pt, and Ta layer is $\sigma_{\text{GdCo}} = (6.31 + 3.78i) \times 10^4$ S/m, $\sigma_{\text{Pt}} = (6.05 + 3.74i) \times 10^5$ S/m, and $\sigma_{\text{Ta}} = (1.43 + 1.96i) \times 10^5$ S/m, respectively.

APPENDIX B: EQUIVALENT CIRCUIT METHOD FOR CALCULATING COMPLEX CONDUCTIVITY OF THE FTF

From Ohm's law, the incident beam with electric field E will induce a current density $j = \sigma E$ in a conducting layer; if the thickness d of the conducting layer is much smaller than its skin depth, the impedance of the conducting layer can be written as $Z = 1/\sigma d$ [30]. For the FTF composed of Pt/GdCo/Pt/Ta, four currents can be induced by the input beam, and the total current corresponds to a current through the four shunting impedances as shown in Fig. 6. Then, the total impedance Z_{FTF} of the FTF can be calculated by the impedance of each layer, which is given by [30]

$$\frac{1}{Z_{\text{FTF}}} = \frac{1}{Z_{\text{Pt}}} + \frac{1}{Z_{\text{GdCo}}} + \frac{1}{Z_{\text{Pt}}} + \frac{1}{Z_{\text{Ta}}}, \quad \textbf{(B1)}$$

where Z_{Pt}, Z_{GdCo}, and Z_{Ta} are the impedance of Pt layer, GdCo layer, and Ta layer, respectively. The complex conductivity of the FTF $\sigma_{\text{FTF}} = 1/(Z_{\text{FTF}} d_{\text{FTF}})$, where d_{FTF} is the total thickness of the FTF. Thus, by changing the thickness of the GdCo alloy, the total thickness of the FTF will be changed, leading to the change of the σ_{FTF}. Figure 2(a) shows the real

Fig. 6. Equivalent circuit mode of the FTF, and the four-layer spin films can be regarded as four parallel circuits.

and imaginary components of the complex conductivity of the FTF as a function of the thickness of GdCo alloy.

APPENDIX C: OPTICAL ABSORPTION OF EACH LAYER OF THE FTF

The optical absorption of each layer of the FTF can be calculated from the ratio of the power dissipated as follows [38]:

$$A = \frac{\int w dV}{0.5 c \varepsilon_0 |E_0|^2 S},$$ (C1)

where $w = 0.5 \varepsilon_0 \omega \varepsilon' |E|^2$ is the power dissipation density, ε' is the imaginary part of the permittivity of the FTF, E is the electric field in the FTF, and E_0 is the electric field of the incident beam on an area S. Figure 2(b) shows the absorption of each layer and the total absorption of the FTF under the different thicknesses of the GdCo alloy.

APPENDIX D: MULTIPLE INTERFERENCE THEORY

When the pump beam with electric field E_0 illuminates the CE-FTF, part of the optical beam will be reflected with a reflection coefficient r_1, and part of the beam will transmit into the SiO$_2$ inserted layer with a transmission coefficient t_1 (Fig. 7). The latter one will continue propagation and be reflected by the Au mirror. Then, it will transmit into the air with a transmission coefficient t_2 or be reflected by the FTF with a reflection coefficient r_2. Thus, the total reflection coefficient of the CE-FTF will be $r = \sum_n E_n / E_0$, where E_n is the electric field of the reflected or transmitted beam, as shown in Fig. 7, and $E_1 = E_0 r_1$, $E_2 = E_0 t_1 r_3 t_2 e^{i2\varphi}$, and $E_3 = E_0 t_1 r_3 r_2 r_3 t_2 e^{i4\varphi}$
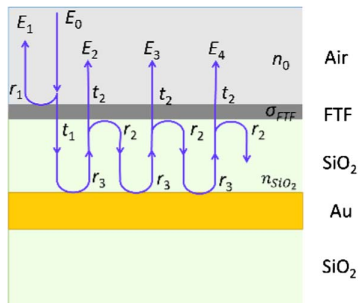
Fig. 7. Schematic of multiple reflections and interference model of the CE-FTF.

[39]. After simplification, the total reflection coefficient of the CE-FTF can be obtained as [40]

$$r = r_1 - \frac{t_1 t_2 e^{i2\varphi}}{1 + r_2 e^{i2\varphi}}.$$ (D1)

## APPENDIX E: TWO-TEMPERATURE MODEL OF THE PHOTOTHERMAL EFFECT

The two-temperature model is applied to simulate the photothermal effect, and the dynamic temperature of the electron and phonon can be calculated. The two-temperature model is described by the following differential equations [17,36]:

$$C_e \frac{dT_e}{dt} = g_{ep}(T_p - T_e) + P(t) - \nu(T_e - T_0),$$ (E1)

$$C_p \frac{dT_p}{dt} = g_{ep}(T_e - T_p),$$ (E2)

$$P(t) = I_0 F e^{-(t/\tau_p)^2}.$$ (E3)

Here, T_p and T_e are the electron and phonon temperatures. g_{ep} is the electron-phonon coupling constant, and it is 4.05×10^{18} W/(m^3 K). T_0 is the room temperature, and it is 298 K. ν is the heat diffusion constant, and it is 100 J/(s m^3 K). C_e and C_p are the electron and phonon heat capacities and $C_e = \gamma T_e$ with $\gamma = 2 \times 10^3$ J/(m^3 K^2),
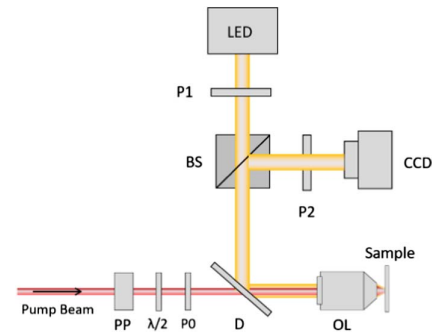
Fig. 8. Static MOKE imaging system. PP, pulse picker; $\lambda/2$, half-wave plate; P0, P1, P2, polarizers; D, dichroscope; BS, beam splitter; LED, light-emitting diode; CCD, charge-coupled device; OL, objective lens.

Fig. 9. Static MOKE images of the PFTF and CE-FTF with $d = 50$, 100, 150, and 200 nm, respectively.

$C_p = 4 \times 10^6$ J/(m^3 K), respectively. I_0 describes the amount of laser energy absorbed by the sample, and $I_0 = 2 \times 10^{20}$ ms^{-1} for the PFTF. F is the laser fluence. τ_p is the laser pulse duration, and it is 35 fs. We should point out that, for the CE-FTF, because the absorption of the pump laser is enhanced, I_0 should be larger during the simulation. According to Figs. 2(a) and 2(c), the I_0 should be larger about 1.46, 1.9, 2.02 and 1.15 times for the four CE-FTFs, respectively. Figure 5 shows the electron and phonon temperatures of the PFTF and the four CE-FTFs under the same fluence. In Fig. 5, we can see that the electron and the phonon temperatures are increased from room temperature to the maximum after the pump of the laser beam; then, they both relax back to room temperature. Within 0.5 ps, T_e can reach its maximum. We can also find that the CE-FTFs have a shorter time to reach the maximum temperature of the electron and phonon higher than the PFTF. Further, the electron and phonon temperatures of the four CE-FTFs are larger than those of the PFTF. Among the four CE-FTFs, the CE-FTF with $d = 150$ nm is the easiest to reach the maximum temperature of the electron and phonon.

APPENDIX F: STATIC MOKE IMAGING SYSTEM

Figure 8 shows the schematic of the home-built static MOKE imaging system. The pump beam comes from an amplified Ti: sapphire laser with repetition rate $f = 1$ kHz, wavelength 780 nm, and pulse duration $t = 35$ fs. The half-wave plate $\lambda/2$ and polarizer P0 are used to tune the pump power.

APPENDIX G: STATIC MOKE IMAGES OF THE PFTF AND CE-FTF

Figure 9 shows the magnetization of the PFTF and the CE-FTF with $d = 50, 100, 150$, and 200 nm after illumination with different laser fluences, respectively.

APPENDIX H: TR-MOKE SYSTEM

Figure 10 shows the schematic of the home-built static TR-MOKE system. The amplified Ti:sapphire laser is employed, and the laser beam is divided into the pump beam and probe beam with a beam splitter. The frequency of the probe beam is doubled by a BBO crystal.
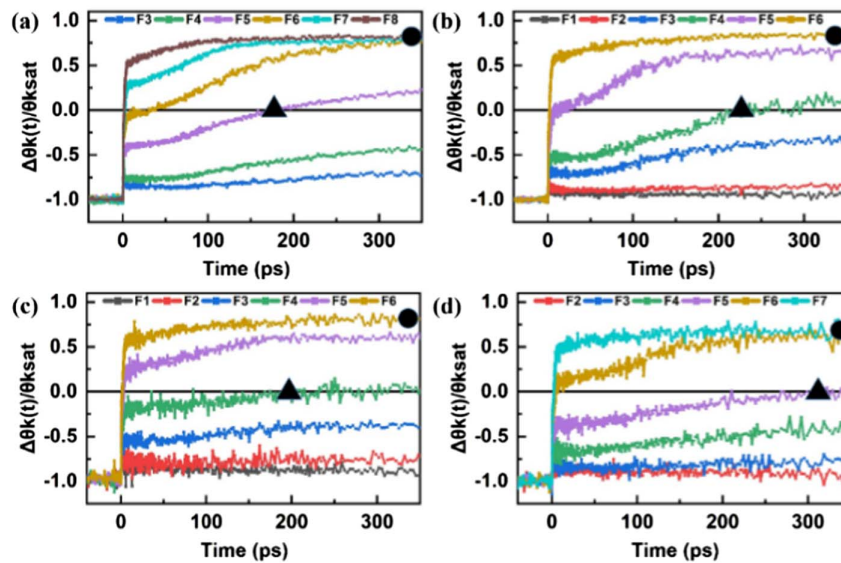
APPENDIX I: NORMALIZED ULTRAFAST MAGNETIZATION DYNAMICS OF THE CE-FTF

Figure 11 shows the normalized ultrafast magnetization dynamics of the CE-FTF with $d = 50, 100, 150, 200$ nm triggered by the pump beam with different fluence.
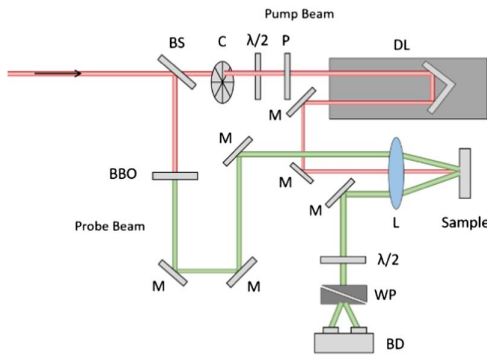
Fig. 10. Time-resolved MOKE (TR-MOKE) system. BS, beam splitter; C, chopper; $\lambda/2$, half-wave plate; P, polarizer; DL, delay line; M, mirror; L, lens; WP, Wollaston prism; BD, balanced detector.

Fig. 11. Normalized ultrafast magnetization dynamics of the CE-FTF with (a) $d = 50$ nm, (b) $d = 100$ nm, (c) $d = 150$ nm, and (d) $d = 200$ nm triggered by the pump beam with different fluence. Here, $F_1 = 0.35$ mJ/cm^2, $F_2 = 0.40$ mJ/cm^2, $F_3 = 0.45$ mJ/cm^2, $F_4 = 0.50$ mJ/cm^2, $F_5 = 0.60$ mJ/cm^2, $F_6 = 0.70$ mJ/cm^2, $F_7 = 0.80$ mJ/cm^2, and $F_8 = 0.90$ mJ/cm^2.

Disclosures.   The authors declare no conflicts of interest related to this article.

Data Availability.   Data underlying the results presented in this paper are not publicly available at this time but may be obtained from the authors upon reasonable request.

REFERENCES

1. B. Dieny, I. L. Prejbeanu, K. Garello, P. Gambardella, P. Freitas, R. Lehndorff, W. Raberg, U. Ebels, S. O. Demokritov, J. Akerman, A. Deac, P. Pirro, C. Adelmann, A. Anane, A. V. Chumak, A. Hirohata, S. Mangin, S. O. Valenzuela, M. C. Onbasli, M. D'Aquino, G. Prenat, G. Finocchio, L. Lopez-Diaz, R. Chantrell, O. Chubykalo-Fesenko, and P. Bortolotti, "Opportunities and challenges for spintronics in the microelectronics industry," Nat. Electron. **3**, 446–459 (2020).
2. S. R. Tauchert, M. Volkov, D. Ehberger, D. Kazenwadel, M. Evers, H. Lange, A. Donges, A. Book, W. Kreuzpaintner, U. Nowak, and P. Baum, "Polarized phonons carry angular momentum in ultrafast demagnetization," Nature **602**, 73–77 (2022).
3. B. C. Stipe, T. C. Strand, C. C. Poon, H. Balamane, T. D. Boone, J. A. Katine, J.-L. Li, V. Rawat, H. Nemoto, A. Hirotsune, O. Hellwig, R. Ruiz, E. Dobisz, D. S. Kercher, N. Robertson, T. R. Albrecht, and B. D. Terris, "Magnetic recording at 1.5 Pb m^{-2} using an integrated plasmonic antenna," Nat. Photonics **4**, 484–488 (2010).
4. N. Zhou, X. Xu, A. T. Hammack, B. C. Stipe, K. Gao, W. Scholz, and E. C. Gage, "Plasmonic near-field transducer for heat-assisted magnetic recording," Nanophotonics **3**, 141–155 (2014).
5. D. O. Ignatyeva, C. S. Davies, D. A. Sylgacheva, A. Tsukamoto, H. Yoshikawa, P. O. Kapralov, A. Kirilyuk, V. I. Belotelov, and A. V. Kimel, "Plasmonic layer-selective all-optical switching of magnetization with nanometer resolution," Nat. Commun. **10**, 4786 (2019).
6. C. H. Lambert, S. Mangin, B. Varaprasad, Y. K. Takahashi, M. Hehn, M. Cinchetti, G. Malinowski, K. Hono, Y. Fainman, M. Aeschlimann, and E. E. Fullerton, "All-optical control of ferromagnetic thin films and nanostructures," Science **345**, 1337–1340 (2014).
7. K. Vahaplar, A. M. Kalashnikova, A. V. Kimel, D. Hinzke, U. Nowak, R. Chantrell, A. Tsukamoto, A. Itoh, A. Kirilyuk, and T. Rasing, "Ultrafast path for optical magnetization reversal via a strongly nonequilibrium state," Phys. Rev. Lett. **103**, 117201 (2009).
8. L. D. Wang, H. Y. Cheng, P. Z. Li, Y. L. W. van Hees, Y. Liu, K. H. Cao, R. Lavrijsen, X. Y. Lin, B. Koopmans, and W. S. Zhao, "Picosecond optospintronic tunnel junctions," Proc. Natl. Acad. Sci. USA **119**, e2204732119 (2022).
9. M. L. M. Lalieu, R. Lavrijsen, and B. Koopmans, "Integrating all-optical switching with spintronics," Nat. Commun. **10**, 110 (2019).
10. P. Z. Li, T. J. Kools, B. Koopmans, and R. Lavrijsen, "Ultrafast racetrack based on compensated Co/Gd-based synthetic ferrimagnet with all-optical switching," Adv. Electron. Mater. **9**, 2200613 (2023).
11. X. Q. Zhang, G. H. Rui, Y. Xu, F. Zhang, Y. C. Du, M. T. Lian, A. T. Wang, H. Ming, and W. Zhao, "Tailoring the magnetic field induced by the first higher order mode of an optical fiber," Opt. Express **28**, 2572–2582 (2020).
12. X. Q. Zhang, G. H. Rui, Y. Xu, F. Zhang, Y. C. Du, X. Y. Lin, A. T. Wang, and W. S. Zhao, "Fully controllable three-dimensions light-induced longitudinal magnetization using a single objective lens," Opt. Lett. **45**, 2395–2398 (2020).
13. S. C. Wang, C. Wei, Y. H. Feng, H. K. Cao, W. Z. Li, Y. Y. Cao, B. O. Guan, A. Tsukamoto, A. Kirilyuk, A. V. Kimel, and X. P. Li, "Dual-shot dynamics and ultimate frequency of all-optical magnetic recording on GdFeCo," Light Sci. Appl. **10**, 8 (2021).
14. S. Mangin, M. Gottwald, C. H. Lambert, D. Steil, V. Uhlir, L. Pang, M. Hehn, S. Alebrand, M. Cinchetti, G. Malinowski, Y. Fainman, M. Aeschlimann, and E. E. Fullerton, "Engineered materials for all-optical helicity-dependent magnetic switching," Nat. Mater. **13**, 286–293 (2014).
15. Y. Liu, H. Cheng, P. Vallobra, H. Wang, S. Eimer, X. Zhang, G. Malinowski, M. Hehn, Y. Xu, S. Mangin, and W. Zhao, "Ultrafast

16. single-pulse switching of Tb-dominant CoTb alloy," Appl. Phys. Lett. **122**, 022401 (2023).
16. X. Y. Lu, X. Zou, D. Hinze, T. Liu, Y. C. Wang, T. Y. Cheng, J. Wu, T. A. Ostler, J. W. Cai, U. Nowak, R. W. Chantrell, Y. Zhai, and Y. B. Xu, "Roles of heating and helicity in ultrafast all-optical magnetization switching in TbFeCo," Appl. Phys. Lett. **113**, 032405 (2018).
17. M. Beens, M. L. M. Lalieu, A. J. M. Deenen, R. A. Duine, and B. Koopmans, "Comparing all-optical switching in synthetic-ferrimagnetic multilayers and alloys," Phys. Rev. B **100**, 220409 (2019).
18. A. Ceballos, A. Pattabi, A. El-Ghazaly, S. Ruta, C. P. Simon, R. F. L. Evans, T. Ostler, R. W. Chantrell, E. Kennedy, M. Scott, J. Bokor, and F. Hellman, "Role of element-specific damping in ultrafast, helicity-independent, all-optical switching dynamics in amorphous (Gd,Tb)Co thin films," Phys. Rev. B **103**, 024438 (2021).
19. M. J. G. Peeters, Y. M. van Ballegooie, and B. Koopmans, "Influence of magnetic fields on ultrafast laser-induced switching dynamics in Co/Gd bilayers," Phys. Rev. B **105**, 014429 (2022).
20. V. Raposo, F. García-Sánchez, U. Atxitia, and E. Martínez, "Realistic micromagnetic description of all-optical ultrafast switching processes in ferrimagnetic alloys," Phys. Rev. B **105**, 104432 (2022).
21. J. Chatterjee, D. Polley, A. Pattabi, H. Jang, S. Salahuddin, and J. Bokor, "RKKY exchange bias mediated ultrafast all-optical switching of a ferromagnet," Adv. Funct. Mater. **32**, 2107490 (2021).
22. J. M. Abendroth, M. L. Solomon, D. R. Barton III, M. S. El Hadri, E. E. Fullerton, and J. A. Dionne, "Helicity-preserving metasurfaces for magneto-optical enhancement in ferromagnetic [Pt/Co]$_N$ films," Adv. Opt. Mater. **8**, 2001420 (2020).
23. F. Cheng, C. Wang, Z. Su, X. Wang, Z. Cai, N. X. Sun, and Y. Liu, "All-optical manipulation of magnetization in ferromagnetic thin films enhanced by plasmonic resonances," Nano Lett. **20**, 6437–6443 (2020).
24. S. Liu, F. Guo, P. Li, G. Wei, C. Wang, X. Chen, B. Wang, W. Zhao, J. Miao, L. Wang, Y. Xu, and X. Wu, "Nanoplasmonic-enhanced spintronic terahertz emission," Adv. Mater. Interfaces **9**, 2101296 (2021).
25. D. Kim, Y. W. Oh, J. U. Kim, S. Lee, A. Baucour, J. Shin, K. J. Kim, B. G. Park, and M. K. Seo, "Extreme anti-reflection enhanced magneto-optic Kerr effect microscopy," Nat. Commun. **11**, 5937 (2020).
26. N. Mou, X. Liu, T. Wei, H. Dong, Q. He, L. Zhou, Y. Zhang, L. Zhang, and S. Sun, "Large-scale, low-cost, broadband and tunable perfect optical absorber based on phase-change material," Nanoscale **12**, 5374–5379 (2020).
27. N. I. Landy, S. Sajuyigbe, J. J. Mock, D. R. Smith, and W. J. Padilla, "Perfect metamaterial absorber," Phys. Rev. Lett. **100**, 207402 (2008).
28. C. Qu, S. Ma, J. Hao, M. Qiu, X. Li, S. Xiao, Z. Miao, N. Dai, Q. He, S. Sun, and L. Zhou, "Tailor the functionalities of metasurfaces based on a complete phase diagram," Phys. Rev. Lett. **115**, 235503 (2015).
29. B. Sensale-Rodriguez, R. Yan, M. M. Kelly, T. Fang, K. Tahy, W. S. Hwang, D. Jena, L. Liu, and H. G. Xing, "Broadband graphene terahertz modulators enabled by intraband transitions," Nat. Commun. **3**, 780 (2012).
30. A. Thoman, A. Kern, H. Helm, and M. Walther, "Nanostructured gold films as broadband terahertz antireflection coatings," Phys. Rev. B **77**, 195405 (2008).
31. A. Andryieuski and A. V. Lavrinenko, "Graphene metamaterials based tunable terahertz absorber: effective surface conductivity approach," Opt. Express **21**, 9144–9155 (2013).
32. J. Zhang, X. Wei, M. Premaratne, and W. Zhu, "Experimental demonstration of an electrically tunable broadband coherent perfect absorber based on a graphene-electrolyte-graphene sandwich structure," Photonics Res. **7**, 868–874 (2019).
33. Y. Xu, M. Hehn, W. Zhao, X. Lin, G. Malinowski, and S. Mangin, "From single to multiple pulse all-optical switching in GdFeCo thin films," Phys. Rev. B **100**, 064424 (2019).
34. Y. Xu, M. Deb, G. Malinowski, M. Hehn, W. Zhao, and S. Mangin, "Ultrafast magnetization manipulation using single femtosecond light and hot-electron pulses," Adv. Mater. **29**, 1703474 (2017).

35. Y. Jiang, X. Zhang, Y. Liu, P. Vallobra, S. Eimer, F. Zhang, Y. Du, F. Liu, Y. Xu, and W. Zhao, "Spintronic terahertz emitter with integrated electromagnetic control," Chin. Opt. Lett. **20**, 043201 (2022).

36. N. Bergeard, M. Hehn, S. Mangin, G. Lengaigne, F. Montaigne, M. L. M. Lalieu, B. Koopmans, and G. Malinowski, "Hot-electron-induced ultrafast demagnetization in Co/Pt multilayers," Phys. Rev. Lett. **117**, 147203 (2016).

37. M. Born and E. Wolf, *Principles of Optics: 60th Anniversary Edition*, 7th ed. (Cambridge University, 2019).

38. Y. M. Qing, H. F. Ma, and T. J. Cui, "Flexible control of light trapping and localization in a hybrid Tamm plasmonic system," Opt. Lett. **44**, 3302–3305 (2019).

39. N. K. Grady, J. E. Heyes, D. R. Chowdhury, Y. Zeng, M. T. Reiten, A. K. Azad, A. J. Taylor, D. A. R. Dalvit, and H.-T. Chen, "Terahertz metamaterials for linear polarization conversion and anomalous refraction," Science **340**, 1304–1307 (2013).

40. H. T. Chen, "Interference theory of metamaterial perfect absorbers," Opt. Express **20**, 7165–7172 (2012).